Primary-Frequency-Tuning and Secondary-Impedance-Matching IPT Converter With Programmable Constant Power Output and Optimal Efficiency Tracking Against Variation of Coupling Coefficient

Bowei Zou, *Graduate Student Member, IEEE*, and Zhicong Huang, *Senior Member, IEEE*

***Abstract*—For inductive power transfer (IPT) systems, load conditions and coupling coefficient are subject to change, and affect system power and efficiency. Aiming at addressing this issue, this article proposes a two-loop control scheme based on a single-stage power-source IPT converter. The proposed IPT converter utilizes a series compensation structure on the primary side and employs a switched-controlled capacitor (SCC) in series with a semiactive rectifier (SAR) on the secondary side. The secondary SCC and the SAR cooperate via an inner control loop to emulate a null secondary impedance and an optimal load resistance, whereas the operating frequency is responsible for the output power regulation via an outer control loop. The operating principle enables programmable constant power (CP) output and optimal efficiency tracking against variations of coupling coefficient and load condition, and all power switches are designed to facilitate soft-switching to reduce switching losses. Moreover, compared with conventional IPT systems that have a constant current or constant voltage output characteristic, programmable CP output characteristics can maximize the output power capability of this IPT converter, which is suitable for battery or supercapacitor charging applications. Finally, simulations and experiments validate the proposed model and method for correctness and feasibility.**

***Index Terms*—Constant power (CP), control loops, dynamic, inductive power transfer (IPT), optimal efficiency.**

I. Introduction

INDUCTIVE power transfer (IPT) is an emerging technology that can transmit power wirelessly without any physical contact. The technology transmits electrical energy from one side of the system to the other side through a loosely coupled magnetic induction link. Due to the absence of direct electrical contact between the load side and the power supply side, there are no exposed metal connectors, which eliminates the risk of sparks and electric shocks [1], [2], and is safer and more reliable as it is not affected by bad weather. Therefore, there are many potential application scenarios of IPT technology, including consumer electronics, biomedical implants, medical electronics, underwater loads, and electric vehicles (EVs) [3], [4], [5], [6], [7], [8], [9], [10].

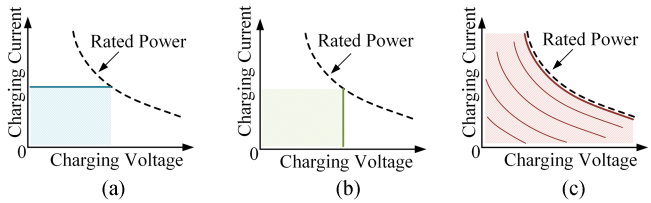

Fig. 1. *V–I* output characteristic curves of IPT converters. (a) Current source. (b) Voltage source. (c) Power source.

Common charging methods for the IPT converter in research include constant current (CC) and constant voltage (CV) profiles [11], [12]. In the IPT system, once the parameters of the loosely coupled transformer (LCT) and the compensation circuit are fixed, the inherent current-source and voltage-source output characteristic of the IPT converter are not adjustable. As a result, the practical application of the IPT converter is significantly restricted by the limited output voltage and current ranges. In general, the maximum transfer capacity of an IPT converter depends on the parameters of the LCT [13], and ideally, there exists a rated maximum output active power without considering reactive power effects as shown by the black dashed line in Fig. 1. Utilizing the inherent current-source or voltage-source output characteristics of the IPT converter, the allowable maximum output voltage and current range is limited by the rated power, as shown in the blue region of Fig. 1(a) and the green region of Fig. 1(b), respectively. Thus, to optimize the power transfer capability of the charging system and improve the charging rate,

Manuscript received 17 October 2023; revised 12 December 2023; accepted 7 January 2024. Date of publication 15 January 2024; date of current version 16 February 2024. This work was supported in part by the National Natural Science Foundation of China under Grant 52007067, in part by the Science and Technology Planning Project of Guangdong Province of China under Grant 2023A0505050124, and in part by the Natural Science Foundation of Guangdong Province of China under Grants 2023A1515011623 and 2022A1515011581. Recommended for publication by Associate Editor K.-B. Park. *(Corresponding author: Zhicong Huang.)*

The authors are with the Shien-Ming Wu School of Intelligent Engineering, South China University of Technology, Guangzhou 510006, China (e-mail: wizoubowei@mail.scut.edu.cn; zhiconghuang@scut.edu.cn).

Color versions of one or more figures in this article are available at https://doi.org/10.1109/TPEL.2024.3353771.

Digital Object Identifier 10.1109/TPEL.2024.3353771

the approach presented in [14] aims to regulate the output voltage and current by maintaining a consistent output power throughout the charging process. This profile is commonly referred to as constant power (CP) charging. The comparison in Fig. 1 shows that when the IPT converter is operated in current-source or voltage-source mode and applied to battery charging, the maximum power is reached only at the rated operating point. If the IPT converter is designed as a power-source system and CP charging is used, as shown in Fig. 1(c), when the IPT converter operates in a cluster of power-source characteristics of the *V*–*I* curve, its output voltage and current range can be broadened to the red region, in order to maximally broaden the output voltage and current range of a single-stage IPT converter, which can be compatible with the charging requirements of different batteries and supercapacitors. Moreover, the application of CP charging as a fast-charging method [15] can contribute to alleviating the issue of battery aging [16], [17].

Compared with stationary scenarios, IPT is more attractive in dynamic scenarios to truly free the power supply, e.g., roadway-powered EVs [18], wireless excited synchronous machines [19], automated guided vehicles [20], etc. However, IPT systems in dynamic scenarios inevitably suffer from more severe parameter fluctuations, and the efficiency and output power of IPT converters are affected by changes in coupling coefficient (k) and load condition. Once it deviates from the optimal load point, it can result in sharp efficiency degradation [21]. In order to deal with the misalignment issue for an IPT system, two main directions can be adopted. First, a passive technology has been adopted, which enables the system to maintain its output characteristics even in the presence of misalignment, without requiring real-time parameter control. By adjusting the structural parameters to optimize the coupling coefficients in the presence of misalignment, it is possible to expand the tolerance for misalignment. For example, rectangular pad [22], bipolar pad [23], [24], tripolar pad [25], and exciter-quadrature-repeaters pad [26] are proposed to achieve high lateral misalignment tolerance. There is other literature that has employed other passive techniques to improve misalignment tolerance [27], [28], [29]. A reconfigurable rectifier-based detuned series–series (S-S) compensated IPT system is proposed to tolerate an extensive coupling [27]. By incorporating a clamping circuit, two additional stable operating regions can be established based on reconfigurable rectifiers, thereby significantly enhancing misalignment tolerance [28]. Some literature has combined two pairs of compensation networks that possess opposite output variations resulting from pad misalignment, thus compensating for one another. This approach is commonly referred to as a hybrid IPT system [30], [31], [32]. Four different connection modes between compensation networks are summarized in [30]. A hybrid topology with primary intermediate coils with CC output characteristics is proposed, with tolerance misalignment performance in both directions [31]. In summary, this class of passive techniques can reduce the efficiency degradation and output fluctuation amplitude of IPT systems to some extent, even in the face of load and magnetic coupling coefficient fluctuations. However, this method is limited in its ability to achieve precise stabilization of the output.

The second approach to deal with the misalignment challenge is to employ an active control system. The principle of this method is to achieve stable output power of the system despite misalignment and variable load conditions by controlling one or multiple variables within the system. Multistage designs have been first carried out to address the above issues [33], [34], [35]. In these designs, an IPT converter is interconnected with a front-end dc–dc converter and a load-side dc–dc converter in a cascaded configuration. Thus, the load-side dc–dc converter is responsible for adaptively adjusting the equivalent load observed by the IPT converter to optimize efficiency, whereas the front-end dc–dc converter utilizes input-side modulation to regulate the output. However, it should be noted that the inclusion of these dc–dc converters introduces additional losses and costs into the system, and moreover, complex control is needed to ensure stability and fast response of the cascading dc–dc converters [36], [37]. In [38], [39], semiactive rectifiers (SARs) are proposed to replace cascaded dc–dc converters. Indeed, although utilizing phase shift control to regulate the primary and secondary sides of the system can potentially reduce the number of converter stages, it is noteworthy that the modulation method of hard switching results in higher switching losses. The soft-switching modulation of voltage-controlled and current-controlled SARs has been studied in [40] and [41]. These SARs transform the load into an equivalent impedance that includes not only a resistive component but also a reactive component. They provide control freedom for load matching but may also worsen the resonance condition in the secondary. Variable frequency modulation (VFM) changes the operating frequency ω to regulate the output power [40], [41] achieving zero voltage switching (ZVS)-ON for switches over a full operating range. However, it cannot cope with the dynamic k variation or misalignment issues, and thus more control freedom is desired for the IPT systems. The switched-controlled capacitor (SCC) technique is found to be another method of compensating reactance in circuits, maintaining the resonance condition of the secondary side through adjustable equivalent capacitance values [44]. Without any modulation in the primary, the proposed wireless power supply in [44] can maintain maximum efficiency against load change but still fails to cope with the issues of dynamic k variation and cannot output a wider power range. In [45], this IPT utilizes the *LCC–LCC* topology and employs both SCCs on both sides, which can output a constant CP when k varies, but it may face challenges in ensuring optimal efficiency tracking when load conditions also vary simultaneously. Hence, achieving the desired output for CP charging and maintaining optimal efficiency in an IPT converter proves to be a challenging task in the presence of variations in the k and load condition.

To address the aforementioned drawbacks, the scheme proposed in this article utilizes a single-stage power-source IPT converter. It introduces a two-loop control scheme that enables optimal efficiency tracking and programmable CP output even when there are simultaneous variations in both the k and load condition. Configuring the equivalent optimal load impedance of the secondary side allows for the achievement of programmable CP output while maintaining optimal efficiency. In addition, all power switches realize soft-switching to mitigate

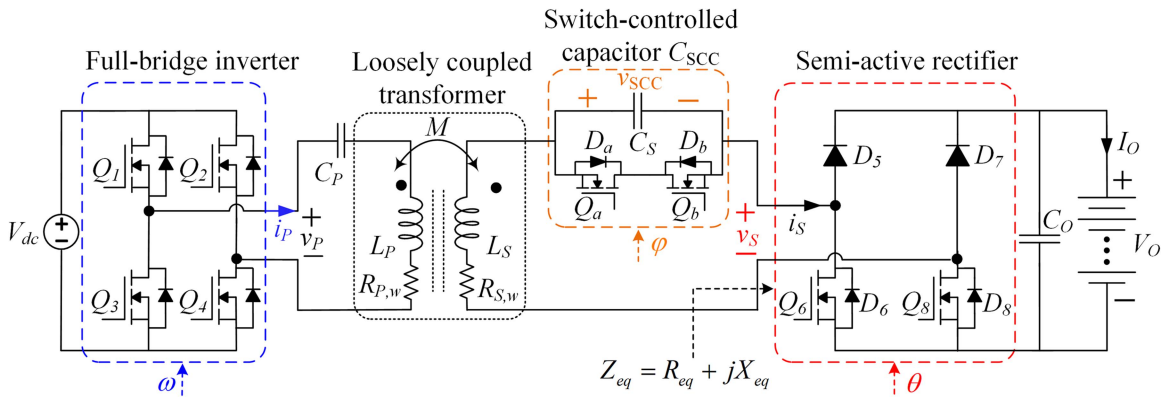

Fig. 2. Schematic of the proposed IPT with programmable CP outputs.

switching losses. The rest of this article is organized as follows. In Section II, the topology and modeling method of the circuit are analyzed. The operating principles of SAR and SCC are introduced, and the equivalent circuit model of the system is obtained. In Section III, the proposed decoupling control loops and output characteristics are introduced in detail, including k-independent criteria for optimal efficiency and regulation of programmable output power. The performances of the proposed IPT converter are experimentally verified in Section IV. Finally, Section V concludes the article.

II. Principle and Analysis

A. System Structure of the Proposed IPT Converter

Fig. 2 shows the proposed wireless programmable CP charger that utilizes an S-S compensated IPT converter, which includes a full-bridge inverter (FBI), an SCC, an LCT, and an SAR. To facilitate referencing, the subscripts P and S are used to denote parameters on the primary and secondary sides, respectively. The LCT consists of self-inductances L_P and L_S with corresponding resistances $R_{P,w}$ and $R_{S,w}$, as well as a mutual inductance M. The coupling coefficient is defined as $k = M/(L_P L_S)^{1/2}$. DC voltage source $V_{\rm dc}$ is modulated into ac voltage v_p with an angular frequency ω, which is then used to drive the primary coil by the FBI with four MOSFET switches Q_1–Q_4. C_P is the primary compensation capacitor with a fixed capacitance value, whereas secondary compensation is accomplished by employing an SCC that is connected in series. The SCC consists of a fixed-value capacitor C_S and two MOSFET switches, namely Q_a and Q_b, along with their corresponding antiparallel body diodes D_a and D_b. By controlling the switching states of Q_a and Q_b, the equivalent variable capacitance $C_{\rm SCC}$ of the SCC can be adjusted accordingly. $v_{\rm SCC}$ is the voltage across the SCC. AC output is rectified to dc output by the SAR with output filter capacitor C_O. The SAR circuit comprises two diodes, namely D_5 and D_7, positioned in the upper legs, whereas the lower legs feature two MOSFET switches identified as Q_6 and Q_8. D_6 and D_8 are the antiparallel body diodes of Q_6 and Q_8, respectively. Secondary ac voltage v_S and ac current i_S are the inputs of the SAR circuit.

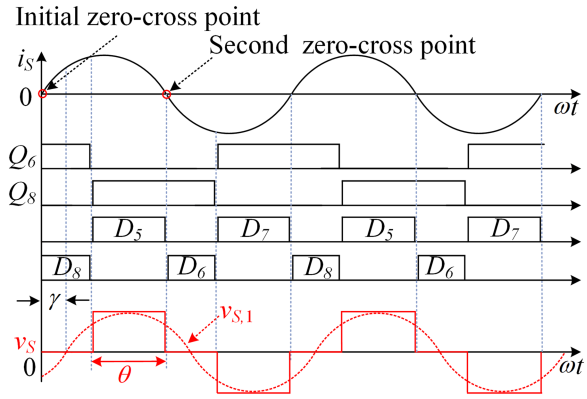

Fig. 3. Switching diagram and modulation scheme of the SAR.

B. Soft-Switched Modulations and Models of SAR and SCC

The switching diagram and modulation scheme of the SAR are shown in Fig. 3. Q_6 and Q_8 are used to control the conduction angle of v_S denoted by θ, and they complement each other in an operating cycle and both only turn ON half a cycle. Taking the initial zero-crossing point as the origin, at this time, i_S is from negative to positive, Q_8 is turned ON with a time delay of $\pi - \theta \in [0, \pi]$, and the conduction time is half a cycle through the second zero-crossing point, at this time, i_S commutates from positive to negative. Q_6 is also turned ON with a time delay of $\pi - \theta \in [0, \pi]$ and the time is half an operating period. Hence, the conduction angle θ of the SAR ranges from a maximum of π to a minimum of 0. Notably, during the ON-time of their respective antiparallel diodes, Q_6 and Q_8 are activated to achieve a ZVS condition. It is noted that any variation in θ directly influences the phase angle between v_S and i_S. Illustrated in Fig. 3, $v_{S,1}$ represents the fundamental component of v_S, exhibiting a lag with respect to i_S. The phase angle between them can be quantified as $\gamma = (\pi - \theta)/2$. Hence, employing this modulation technique allows the input impedance of the SAR to be matched with the requisite impedance of the converter. Therefore, its equivalent load is an impedance rather than a pure resistance, as given by (1)–(3). The derivation can be found in [40], [44], and [46]. Given that the charging of the battery is considerably slower

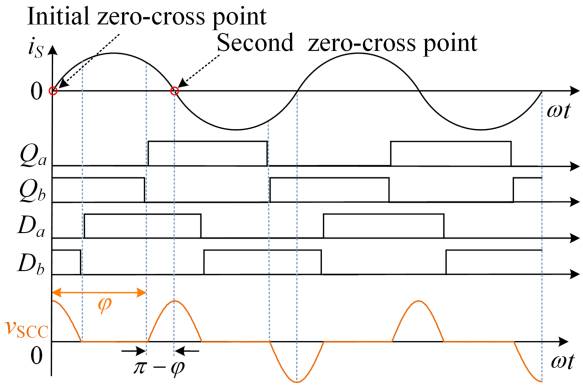

Fig. 4. Switching diagram and modulation scheme of the SCC.

when contrasted with the operational period of the CP source IPT converter, a resistor model is utilized to represent the battery. Specifically, this model incorporates the charging voltage and charging current, i.e., $R_L = V_O/I_O$

$$Z_{\text{eq}} = R_{\text{eq}} + jX_{\text{eq}} \tag{1}$$

where

$$R_{\text{eq}} = \frac{8}{\pi^2} R_L \sin^4\left(\frac{\theta}{2}\right) \tag{2}$$

and

$$X_{\text{eq}} = -\frac{8}{\pi^2} R_L \sin^3\left(\frac{\theta}{2}\right) \cos\left(\frac{\theta}{2}\right) \tag{3}$$

are equivalent resistance and capacitive reactance, respectively.

The concept of SCC was first proposed in [47], which is a special circuit topology combining switching devices and capacitors. Its operating principle is to control the ON–OFF of the switching device to achieve desired outcomes. Then, the charging time (or discharging time) of the C_S in half a cycle is $\pi - \varphi$, which decreases with the increase of φ and leads to the decrease of the equivalent root-mean-square value of v_{SCC}. Consequently, the equivalent capacitance C_{SCC} of the SCC can be varied by the phase shift angle φ. The switching diagram and modulation scheme of the SCC are shown in Fig. 4. Both Q_a and Q_b are turned ON for one-half of the operating cycle, and they are complements of each other. Taking the initial zero-crossing point as the origin, at this time, i_S is from negative to positive, Q_a is turned ON with a time delay of $\varphi \in [\pi\ /\ 2,\ \pi]$, and the conduction time is half a cycle through the second zero-crossing point, when i_S commutates from positive to negative. Q_b is also turned ON with a time delay of $\varphi \in [\pi\ /\ 2,\ \pi]$ and the time is half an operating period. Turning ON Q_a and Q_b at zero voltage enables soft switching, which helps minimize switching losses in the system. Research has shown that the equivalent variable capacitance C_{SCC} can be calculated by considering the fundamental components of i_S and v_{SCC} [47], [48]. The capacitive reactance donated by C_{SCC} is highlighted as (4), and it can be simplified as a polynomial given by (5) for easy

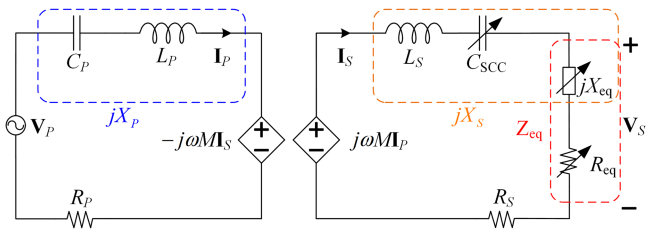

Fig. 5. Equivalent mutual inductance circuit model.

calculation

$$X_{C_{\text{SCC}}} = \left(2 - \frac{2\varphi - \sin 2\varphi}{\pi}\right) X_{C_S} \tag{4}$$

$$\approx \frac{4(\varphi - \pi)^2}{\pi^2} X_{C_S} \tag{5}$$

where $X_{C\text{SCC}} = -1/(\omega C_{\text{SCC}})$, $X_{CS} = -1/(\omega C_S)$. The control loops proposed in this article not only operate at the resonance point but the capacitance value C_S of the SCC should be selected to meet the system requirements over the entire frequency range. To make the key contents more concise, a detailed evaluation is given in the Appendix.

C. Equivalent Circuit Model of the Proposed IPT Converter

Fig. 5 presents the equivalent circuit model of the proposed system, employing the fundamental approximation. It is noteworthy that the equivalent circuit model of the proposed converter is similar to the conventional S-S IPT converter, except that the secondary side compensation capacitor and load impedance are adjustable and the operating frequency ω is not limited to the resonant frequency, i.e., variable C_{SCC}, Z_{eq}, and ω. In addition, the equivalent impedance Z_{eq} is composed of resistance R_{eq} and reactance X_{eq} in series. v_P, i_P, v_S, and i_S are fundamental components, and $\mathbf{V}_P$, $\mathbf{I}_P$, $\mathbf{V}_S$, and $\mathbf{I}_S$ are vector representations of fundamental components, respectively. The resistance R_P is the parasitic resistance from the primary coil and the inverter. Similarly, resistor R_S includes losses arising from the secondary coil, the SCC, and the SAR. When Kirchhoff's voltage law is applied to the equivalent model, the resultant relationship can be expressed as follows:

$$\mathbf{V}_P = \mathbf{I}_P (jX_P + R_P) - jX_M \mathbf{I}_S \tag{6}$$

and

$$jX_M \mathbf{I}_P = \mathbf{I}_S (jX_S + R_S + R_{\text{eq}}) \tag{7}$$

where

$$X_P = \omega L_P - \frac{1}{\omega C_P} \tag{8}$$

$$X_S = \omega L_S - \frac{1}{\omega C_{\text{SCC}}} + X_{\text{eq}} \tag{9}$$

and

$$X_M = \omega M. \tag{10}$$

III. Proposed Method and Output Characteristics

A. k-Independent Criteria for Optimal Efficiency

The power transfer dc-to-dc efficiency η of the circuit model is defined as the ratio of the output active power to the input active power, based on this definition the efficiency expression of the system can be obtained as (11). By substituting (6)–(10) into (11), η can be expressed by (12). As a high-quality IPT converter usually satisfies $X_M^2/(R_P R_S) >> 1$ and $R_{\rm eq}/R_S >> 1$ [44], (12) can be further simplified as (13)

$$\eta = \frac{|\mathbf{I}_S|^2 R_{eq}}{|\mathbf{I}_S|^2 (R_{eq}+R_S) + |\mathbf{I}_P|^2 R_P} \tag{11}$$

$$= \frac{X_M^2 R_{eq}}{\left[(R_{eq}+R_S)^2 + X_S^2\right] R_P + X_M^2 (R_{eq}+R_S)} \tag{12}$$

$$\approx \frac{1}{\frac{R_{eq}+\frac{X_S^2}{R_{eq}}}{X_M^2} R_P + \frac{R_S}{R_{eq}} + 1}. \tag{13}$$

Optimal values of $R_{\rm eq}$ and X_S for achieving optimal efficiency can be found directly according to (13). Given a chosen operating frequency ω, by solving the partial differential $\partial\eta/\partial X_S = 0$ and $\partial\eta/\partial R_{\rm eq} = 0$, optimal efficiency $\eta_{\max}$ can be obtained as

$$\eta_{\rm opt} \approx \frac{1}{\frac{2}{\frac{X_M}{\sqrt{R_P R_S}}} + 1} \tag{14}$$

if

$$X_S, {\rm opt} = \omega L_S - \frac{1}{\omega C_{SCC}} + X_{eq} = 0 \tag{15}$$

and

$$R_{\rm eq,opt} = X_M \sqrt{\frac{R_S}{R_P}}. \tag{16}$$

As can be inferred from (14) to (16), the system efficiency remains unaffected by the primary equivalent reactance X_P. Thus, in the proposed topology, even when VFM is employed, optimal efficiency can still be achieved by ensuring that the secondary resonant tank exhibits null equivalent reactance, and the equivalent load resistance is properly matched.

From (15), null secondary reactance can be maintained by varying $C_{\rm SCC}$ to offset $X_{\rm eq}$. From (16), it is evident that the $R_{\rm eq}$ is dependent on the k, and as such, it should be adjusted accordingly to achieve optimal efficiency in dynamic scenarios. However, due to the inherent difficulty in directly measuring k in practical applications, it is imperative to derive a feasible criterion for attaining optimal efficiency. Assuming the condition of null secondary reactance, as indicated by the satisfaction of (15), the amplitude ratio of secondary side current to primary side current can be defined as

$$\alpha = \left|\frac{\mathbf{I}_S}{\mathbf{I}_P}\right| = \frac{X_M}{(R_{eq}+R_S)}. \tag{17}$$

The variables that influence the current ratio α can be noted from (17), which include mutual inductance and load equivalent values. Among these considerations, the equivalent resistance of the secondary side R_S is small in comparison to the load equivalent resistance $R_{\rm eq}$, and therefore it can be neglected. When the converter satisfies the condition of optimal efficiency, i.e., satisfies (15), (16). By substituting $X_{S,\rm opt}$ and $R_{\rm eq,opt}$ into (17), the optimal $\alpha_{\rm opt}$ can be derived as

$$\alpha_{\rm opt} = \left|\frac{\mathbf{I}_S}{\mathbf{I}_P}\right| \approx \frac{X_M}{R_{\rm eq,opt}} = \sqrt{\frac{R_P}{R_S}}. \tag{18}$$

Here, (18) presents the k-independent criterion, which allows for optimal efficiency to be achieved regardless of the value of k. As depicted in Fig. 6, the IPT converter always operates at optimal efficiency under different k if α is maintained at $\alpha_{\rm opt}$. Since the current amplitudes can be readily detected, (18) is a viable condition for tracking the optimal efficiency.

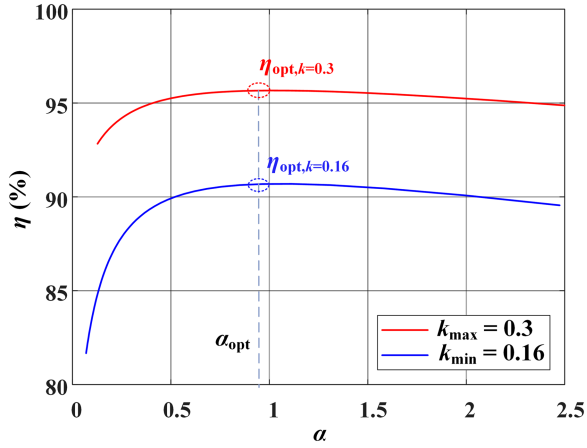

Fig. 6. DC-to-DC efficiency η versus current ratio α under different values of k. (Parameters used for simulation are: $L_P = 147.23$ μH, $L_S = 148.5$ μH, $R_P = 0.451$ Ω, and $R_S = 0.52$ Ω. Unless specified, they will be used for the rest simulation.)

B. Programmable CP Output

In addition to maintaining optimal efficiency, a wide range of output power is desired in dynamic IPT to accommodate the different battery modules and supercapacitors. Since the secondary modulation is responsible for optimal efficiency, we propose a two-loop control scheme to ensure the output power requirements. Assuming $R_P = R_S = 0$, i.e., lossless power transfer, the output power is given by

$$P_O = \left|\frac{\mathbf{I}_S}{\sqrt{2}}\right|^2 R_{\rm eq,opt} = \frac{|\mathbf{V}_P|^2 X_M}{2\left(X_P^2 + X_M^2\right)}. \tag{19}$$

Here, P_O can be regulated by the operating frequency ω, whereas the converter ensures optimal efficiency. Fig. 7 shows the output power P_O together with the primary reactance X_P along with the variation of operating frequency ω. Wide-range output power can be readily achieved by varying ω.

C. Inner Loop Control for Optimal Efficiency

The primary objective of the inner loop control is to optimize the transmission efficiency of the converter. The attainment of impedance matching is considered pivotal in accomplishing this

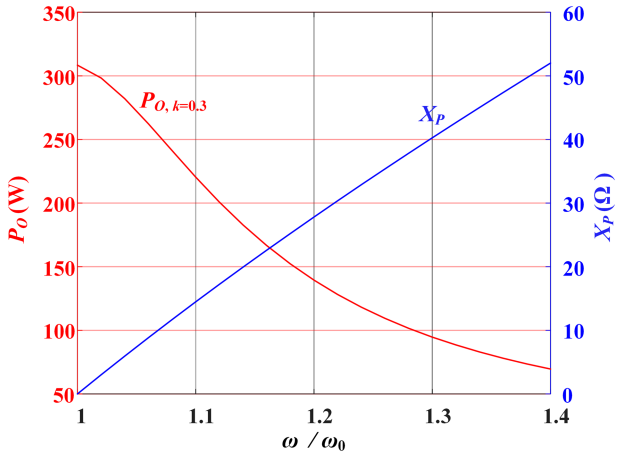

Fig. 7. Output power P_O and primary reactance X_P versus operating frequency ω.

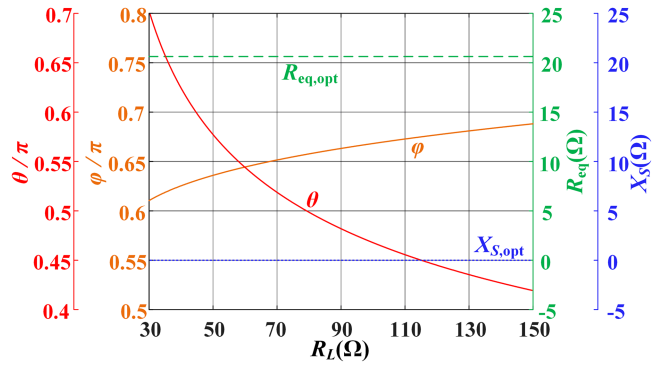

Fig. 8. φ, θ, $R_{\rm eq}$, and X_S versus R_L ($k = 0.3$).

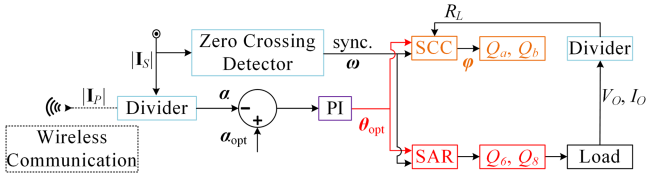

Fig. 9. Inner loop optimal efficiency control diagram.

objective. The SAR is responsible for transforming R_L into $R_{\rm eq,opt}$ by varying the conduction angle θ of the SAR. The change of the magnetic coupling coefficient in the dynamic IPT leads to the change of the optimal matching load. However, it is difficult to observe $R_{\rm eq,opt}$ directly. Alternatively, as demonstrated in Section III-A, it is straightforward to observe the current ratio α, and once α is tightly regulated as $\alpha_{\rm opt} \approx (R_P R_S)^{1/2}$ given in (18), $R_{\rm eq,opt}$ can be achieved regardless of k variation. Therefore, θ is controlled for the achievement of $\alpha_{\rm opt}$.

Moreover, by solving the partial differential given in (20), it can be found that α monotonically decreases with the increase of θ, such that, a linear controller can be used to regulate θ

$$\frac{\partial \alpha}{\partial \theta} = -\frac{\pi^2 X_M}{16 R_L \sin^5\left(\frac{\theta}{2}\right)} < 0, (\theta \in [0, \pi]). \tag{20}$$

In practice, $\alpha_{\rm opt}$ should be precisely evaluated by including the losses of all switches into consideration. With the experimental parameters listed in Section IV, the actual $\alpha_{\rm opt}$ of the experimental prototype is around 0.95. Therefore, $\alpha_{\rm opt} = 0.95$ is used as the control reference.

From (1), it can be seen that a capacitive impedance $X_{\rm eq}$ is inevitably generated during the SAR regulation process, and the control purpose of the secondary SCC is to cancel the equivalent load reactance $X_{\rm eq}$ generated by the SAR and maintain null reactance in the secondary. Therefore, it is necessary to explore the coordinative control of φ and θ. With (3), (5), and (15), the expression of phase-shift angle φ can be derived as (21). Here, φ can be uniquely determined for particular values of θ and R_L. This means that the control variables θ and φ can only be considered as one control variable

$$\varphi = \pi - \frac{\pi}{2}\sqrt{C_S\left(\omega^2 L_S - \frac{U_O}{I_O}\omega\frac{8}{\pi^2}\sin^3\frac{\theta}{2}\cos\frac{\theta}{2}\right)}. \tag{21}$$

Based on the above analysis, as depicted in Fig. 8, the cooperation of the SAR and the secondary SCC meets the requirements of optimal efficiency under variations of load conditions when $k = 0.3$. The diagram of inner loop control can be designed and implemented as shown in Fig. 9. First, the sensor can be employed to measure the output voltage V_O and output current I_O. Meanwhile, the divider can be utilized to calculate the value of R_L. Current transformers, along with rectifiers, are employed to sample $|\mathbf{I}_P|$ and $|\mathbf{I}_S|$, which are converted into dc values. Wireless communication is utilized to transmit the $|\mathbf{I}_P|$ value from the primary to the secondary side for the calculation of α. To make adjustments based on the disparity between α and $\alpha_{\rm opt}$, a straightforward proportional–integral (PI) controller is implemented. The PI controller generates the control signal, which is denoted as the conduction angle θ, for the SAR. After determining θ and R_L, another control signal φ, referred to as the control angle of the SCC, is computed and generated using the analytical relationship provided in (21), as shown in Fig. 8. The φ is adjusted to keep the secondary side circuit in resonance and optimize the system efficiency. Combined with Figs. 3 and 4, zero-crossing detection of i_S generates a synchronization signal for the pulsewidth modulation (PWM) generations, and the operating frequency ω of the converter is calculated simultaneously using this mechanism. Subsequently, based on the synchronous signal generated, angles φ and θ are utilized to produce PWM driving signals for the SCC and SAR, respectively, to complete the coordinated control process of the secondary side.

D. Outer Loop Control for CP Output

On the basis of the inner loop, an outer loop is added, which is responsible for correcting the P_O when k changes by modulating the operating frequency ω. Taking the experimental platform rated at 308 W as an example, assuming that the operating frequency is the resonant frequency, it is known from (19) that the converter output power varies with k as shown in the red curve in Fig. 10. Therefore, in conjunction with Fig. 7, from

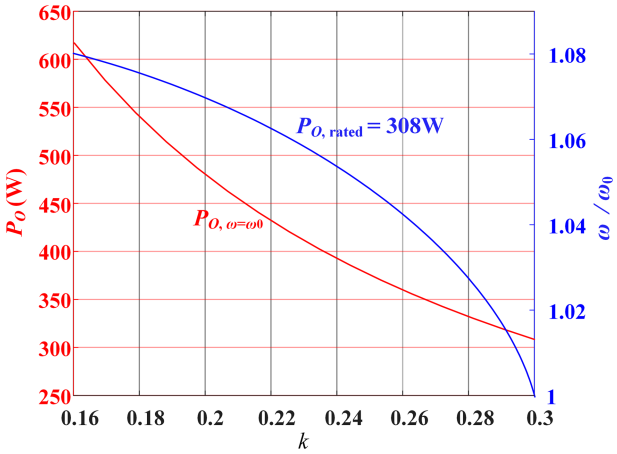

Fig. 10. Output power P_O and operating frequency ω versus k.

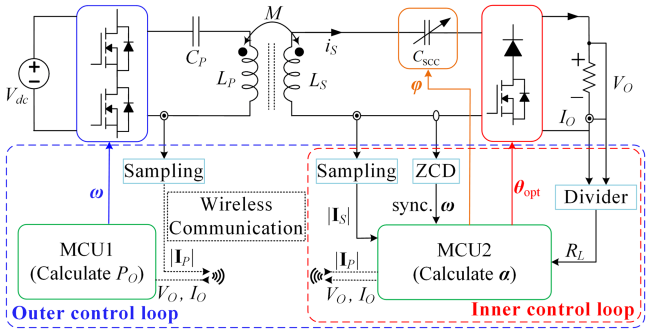

Fig. 11. Diagram control diagram of the proposed IPT converter.

(19), the operating frequency ω should be tightly regulated to maintain a CP output against the variations of k and load condition. Solving the partial differential (22) shows that P_O exhibits a monotonically decreasing trend with an increase in ω. In the case of varying k, the frequency is adjusted to maintain the output power at the rated power level, as shown in the blue curve in Fig. 10

$$\frac{\partial P_O}{\partial \omega} = \frac{|\mathbf{V}_P|^2 M}{2}\left[\frac{1}{X_P^2+X_M^2} - \frac{2\omega X_P\left(L_P+\frac{1}{\omega^2 C_P}\right)+2X_M M}{\left(X_P^2+X_M^2\right)^2}\right]. \tag{22}$$

Fig. 10 shows the simulated curves of P_O versus k and validates the monotonicity. Therefore, the design and implementation of the outer loop control diagram can be depicted as shown in Fig. 11. Another PI controller is readily implemented to regulate the output power in the outer control loop. On the secondary side, the dc values of V_O and I_O are sampled and subsequently multiplied to obtain P_O. P_O is wirelessly transmitted back to the primary side. In order to maintain the desired power level, a PI controller compares the actual value of P_O with its reference value $P_{O,\text{ref}}$. The output of the PI controller is utilized to adjust the operating frequency ω for the primary FBI.

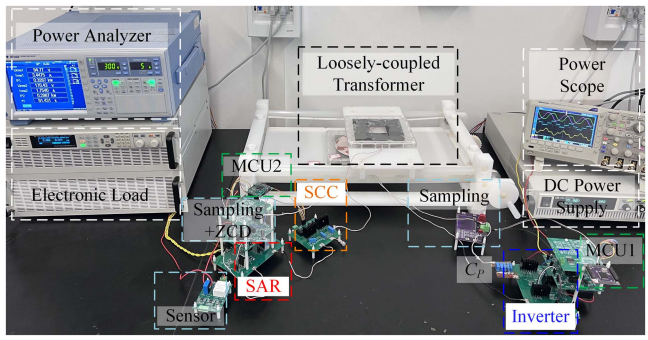

Fig. 12. Experimental prototype.

TABLE I
BASIC SYSTEM PARAMETERS

Parameters	Symbols	Measured values
DC input voltage	V_{dc}	95 V
Rated output power	$P_{\text{O,rated}}$	308 W
Switches	Q_1–Q_4, Q_a, Q_b, Q_6, Q_8	SCT4045DR with $R_{\text{on}} \approx 0.045\ \Omega$ and $V_{\text{F}} \approx 3.0$ V
Diodes	D_5, D_7	MBR20200CT with $V_{\text{F}} \approx 0.9$ V
Self-inductance	L_P, L_S	147.23 μH, 148.5 μH
Coil resistance	$R_{P,w}$, $R_{S,w}$	0.246 Ω, 0.3 Ω
Coupling coefficient	k	0.16–0.3
Primary compensation	C_P	25.68 nF
Secondary compensation	C_S	12.6 nF
Operating frequency	$\omega/2\pi$	82–114.8 kHz
Load	R_L	30–150 Ω
Number of turns	N	34
Inner diameter	d_i	34 mm
Outer diameter	d_o	152 mm
Air gap distance	g	35 mm

IV. EXPERIMENTAL VERIFICATION

In order to validate the optimal efficiency tracking and programmable CP output against variations of k and load condition, a practical experimental prototype is constructed, as shown in Fig. 12. The experimental prototype includes a dc power supply, FBI, primary side series resonant network, LCT, secondary side SCC, SAR, sampling circuits, control circuits, a power analyzer, and an electronic load. The system parameters are listed in Table I. The primary side pad is fixed, whereas the horizontal displacement between the secondary side pad and

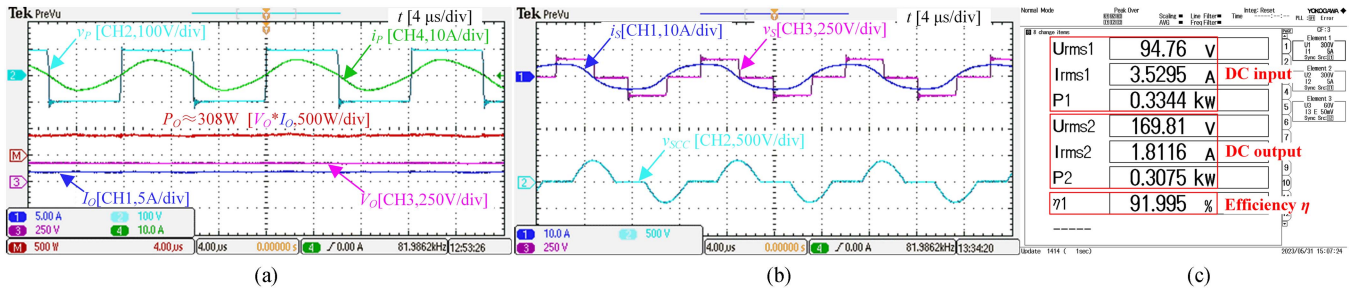

Fig. 13. Captured steady-state waveforms under $P_{O,\mathrm{ref1}} = 308$ W. The coupling coefficient is $k = 0.3$, $R_L = 90\ \Omega$. (a) Operating waveforms of the inverter, and the dc output. (b) Operating waveforms of the SCC, and the SAR. (c) Screen capture of DC-to-DC efficiency measurement.

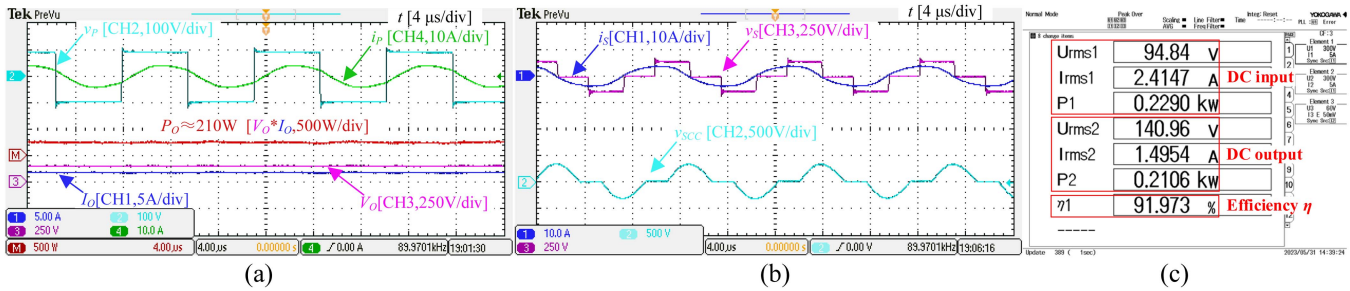

Fig. 14. Captured steady-state waveforms under $P_{O,\mathrm{ref2}} = 210$ W. The coupling coefficient is $k = 0.3$, $R_L = 90\ \Omega$. (a) Operating waveforms of the inverter, and the dc output. (b) Operating waveforms of the SCC, and the SAR. (c) Screen capture of DC-to-DC efficiency measurement.

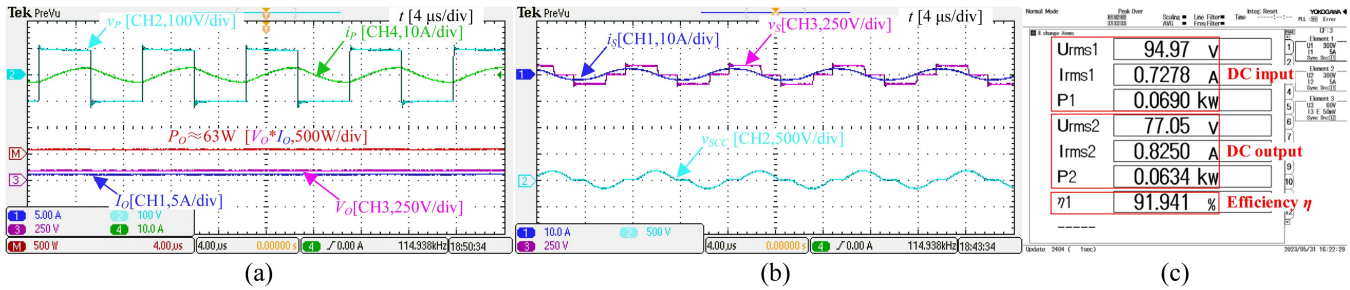

Fig. 15. Captured steady-state waveforms under $P_{O,\mathrm{ref3}} = 63$ W. The coupling coefficient is $k = 0.3$, $R_L = 90\ \Omega$. (a) Operating waveforms of the inverter, and the dc output. (b) Operating waveforms of the SCC, and the SAR. (c) Screen capture of DC-to-DC efficiency measurement.

the primary side pad is adjusted by rotating the rocker. The displacement ranges from 0 to 52 mm, and the coupling coefficient k varies from 0.3 to 0.16 correspondingly. The load resistance is emulated by an electronic load. The system efficiency is measured by Yokogawa WT1803E precision power scope.

A. Programmable CP Output

Without loss of generality, the coupling coefficient is set at $k = 0.3$ to capture the steady-state waveforms. Figs. 13–15 show them under different reference powers. With the same load resistance $R_L = 90\ \Omega$, due to the standards of different operating conditions, it is necessary to provide different levels of CP output to achieve the target requirement. Set reference output power $P_{O,\mathrm{ref1}} = 308$ W as shown in Fig. 13(a). It can be seen that the phase between v_p and i_p are the same and the system frequency is the resonant frequency ω_0. As shown in Fig. 14(a), set the reference output power $P_{O,\mathrm{ref2}} = 210$ W for the system output; as shown in Fig. 15(a), set the reference output power $P_{O,\mathrm{ref3}} = 63$ W for the system output. It can be seen that the phase of v_p is ahead of i_p, the operating frequency ω is higher than the resonant frequency, and the primary side presents inductive impedance. Comparison of Figs. 13–15 shows that the modulation strategy proposed in Section III-B enables the converter to output different levels of power. The experimental results verify the programmable power source output characteristics of the proposed control loops. The conduction angle θ of the SAR and phase-shift angle φ of the secondary SCC can be observed in Figs. 13(b)–15(b). The waveforms are therefore

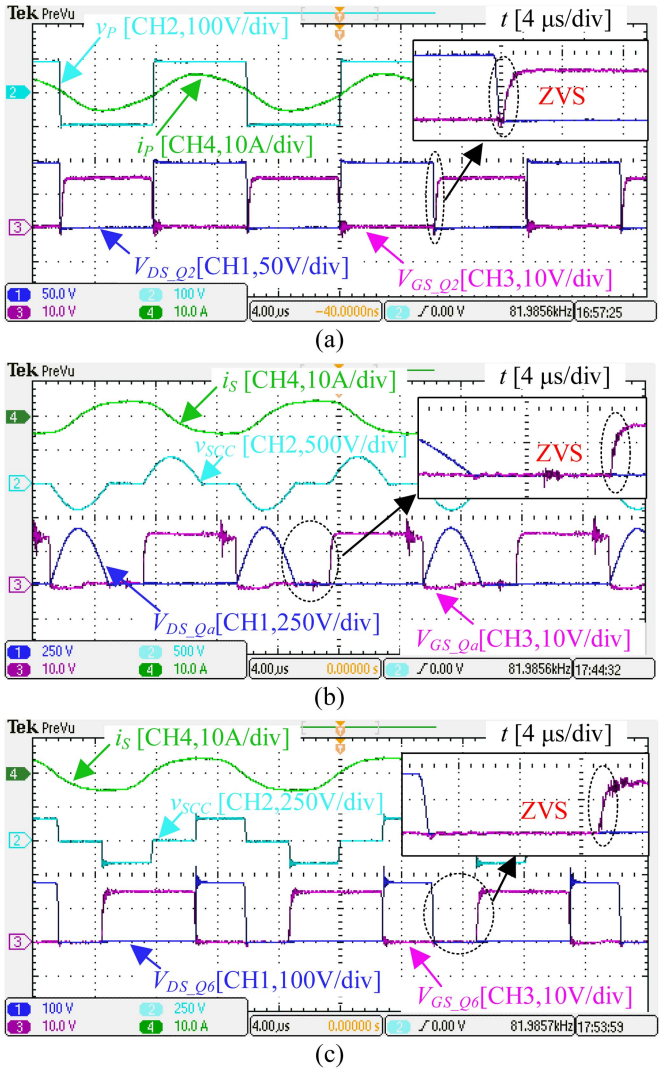

Fig. 16. Soft switching characteristics of each part at different frequencies, $f_0 = 82$ kHz. (a) Q_2 of FBI. (b) Q_a of SCC. (c) Q_6 of SAR.

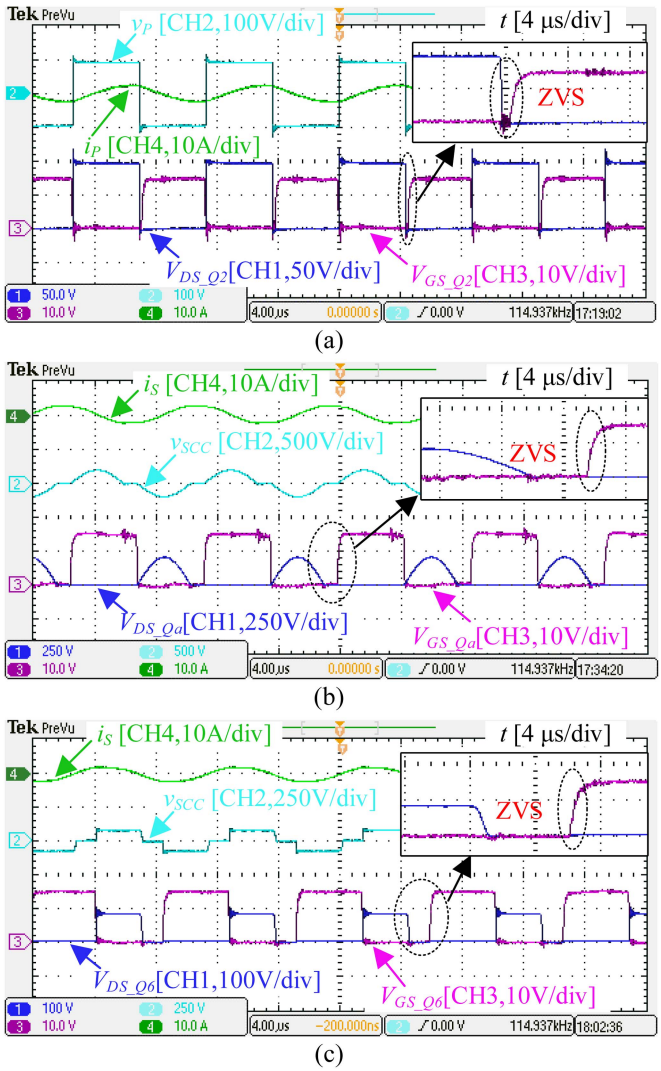

Fig. 17. Soft switching characteristics of each part at different frequencies, $f_1 = 114.8$ kHz. (a) Q_2 of FBI. (b) Q_a of SCC. (c) Q_6 of SAR.

consistent with the operating principle illustrated in Section II-B. To validate the soft switching characteristics of all components using the proposed control strategy, the switching waveforms of each switch part (FBI, SCC, SAR) at different frequencies when $k = 0.3$ are depicted in Figs. 16 and 17. CH2 and CH4 represent the voltage and current of the respective part, whereas CH1 and CH3 illustrate the voltage waveforms between the drain–source and the corresponding gate–source driving signals of one of the switches in the three parts, respectively. The waveforms in Figs. 16 and 17 demonstrate soft switching for the primary FBI through frequency modulation, whereas the SCC and SAR on the secondary side exhibit effortless soft switching. Consequently, zero-voltage switching can be realized for each component of the switch. In addition, from Figs. 13(c) to 15(c), as analyzed in Section III-A, even though the operating frequency ω is not at the resonance point, the efficiency of the converter dc–dc is maintained at the optimum efficiency, which is above 91.9%, if both (15) and (16) are satisfied.

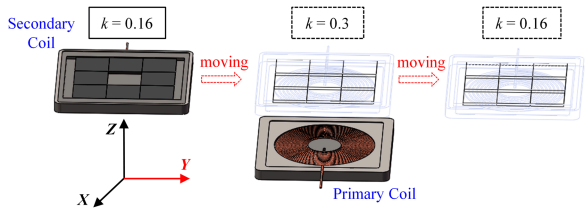

Fig. 18. Schematic of the displacement between the secondary pad and primary pad.

B. Transient Waveforms Under Changing Coupling

As shown in Fig. 18, the coupling coefficient k is varied from 0.3 to 0.16 and back to 0.3 by slowly changing the displacement of the secondary pad to the primary pad. The transient waveforms under varying coupling coefficients in different load conditions are shown in Figs. 19–21. Similarly, the primary side ac voltage v_p, ac current i_p, and secondary side ac current i_S are measured, corresponding to CH2, CH4, and CH1, respectively.

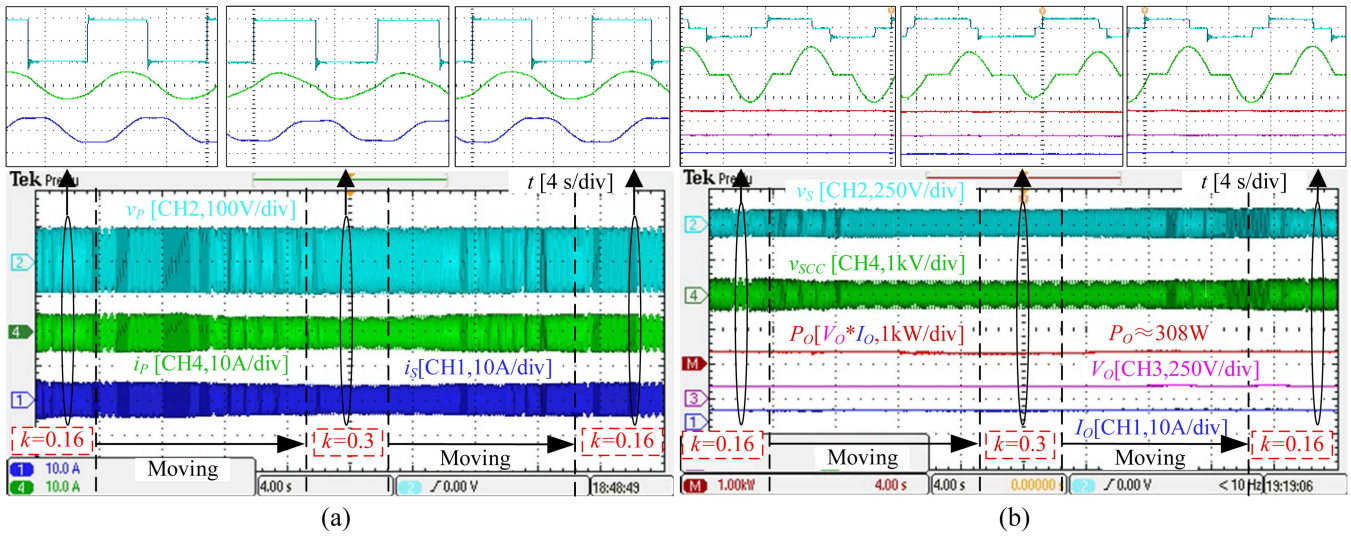

Fig. 19. Transient waveforms against variation of coupling coefficient under different load conditions, $R_L = 30\ \Omega$.

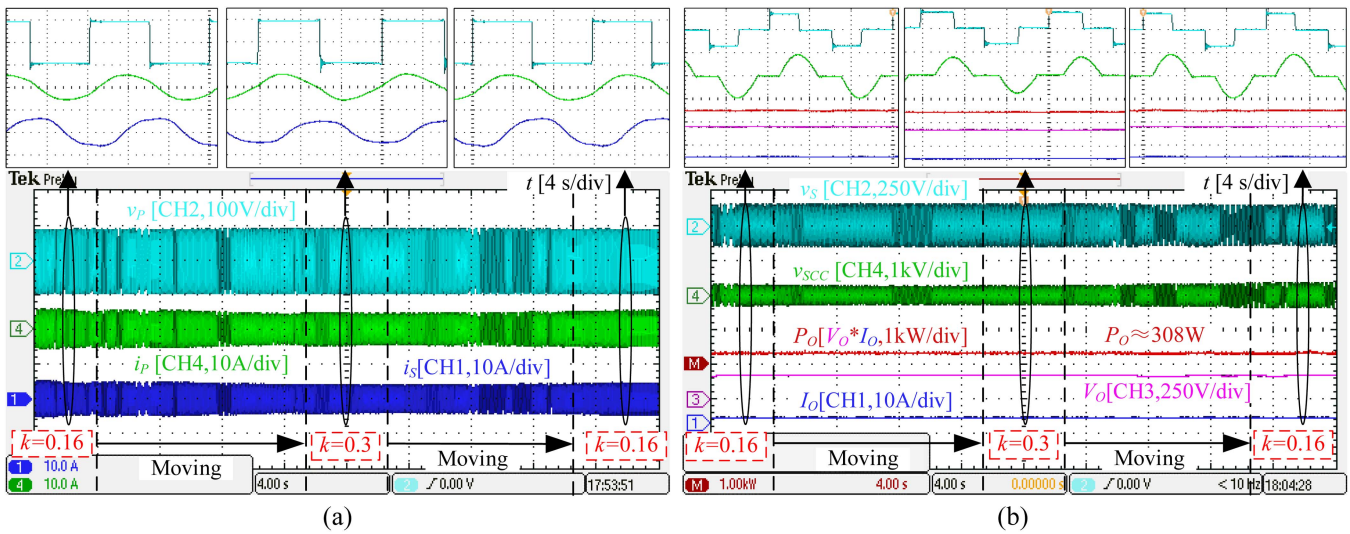

Fig. 20. Transient waveforms against variation of coupling coefficient under different load conditions, $R_L = 90\ \Omega$.

The amplified waveforms facilitate the observation of the current amplitude ratio in the control mentioned in Section III-A. By comparing the waveforms under distinct coupling states, it can be observed that the current ratio α controlled by the inner loop is tightly regulated to 0.95, aiming to optimize the efficiency of the converter. In addition, the ac voltage v_S of the secondary side, the voltage v_{SCC} of the SCC, the dc output voltage V_O, and the dc output current I_O are measured, corresponding to CH2, CH4, CH3, and CH1, respectively. The waveform in red represents the calculated P_O, obtained by multiplying the V_O and I_O waveforms. Comparing the waveforms under different coupling states, it is evident that the output power P_O is tightly regulated as 308 W via the outer loop control. From Figs. 19–21, it is verified that the proposed wireless CP converter achieves a CP output and tracks the optimal efficiency despite variations in the k.

C. Transient Waveforms Under Changing Load

The transient waveforms against step load change under different values of k are shown in Fig. 22. The primary side ac current i_p, secondary side ac current i_S, the dc output voltage V_O, and the dc output current I_O are measured and shown by CH4, CH2, CH3, and CH1, respectively. The waveform in red represents P_O, which is determined by multiplying V_O and I_O waveforms. The load resistance is step changed from 30 to 90 Ω and back to 30 Ω again. By amplifying the waveform, it can be seen that the current ratio is tightly regulated against step load

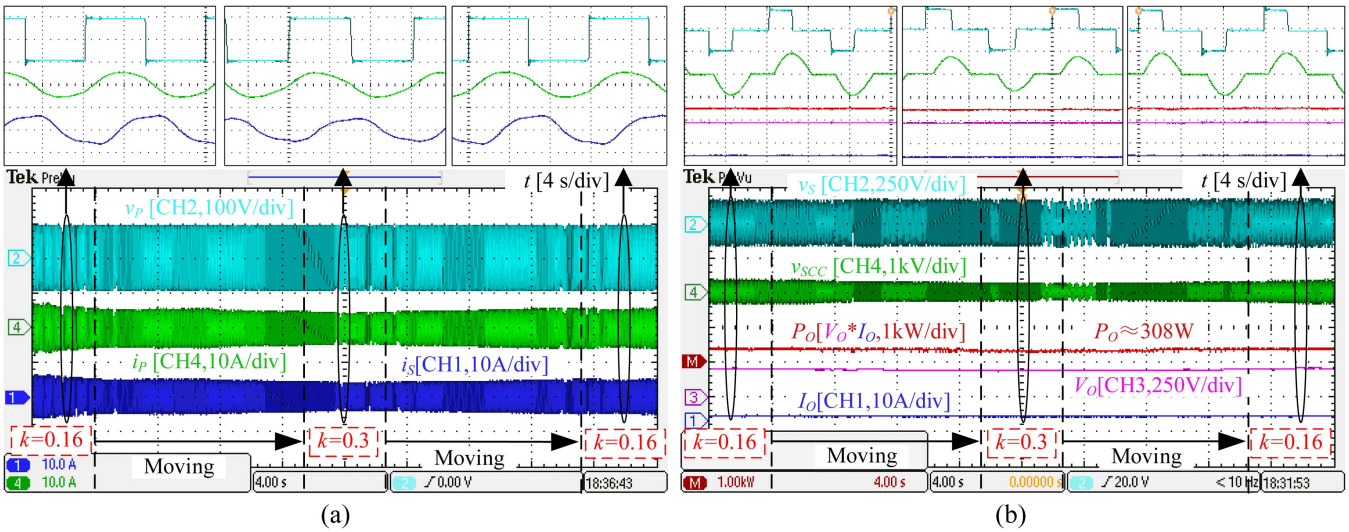

Fig. 21. Transient waveforms against variation of coupling coefficient under different load conditions, $R_L = 150\ \Omega$.

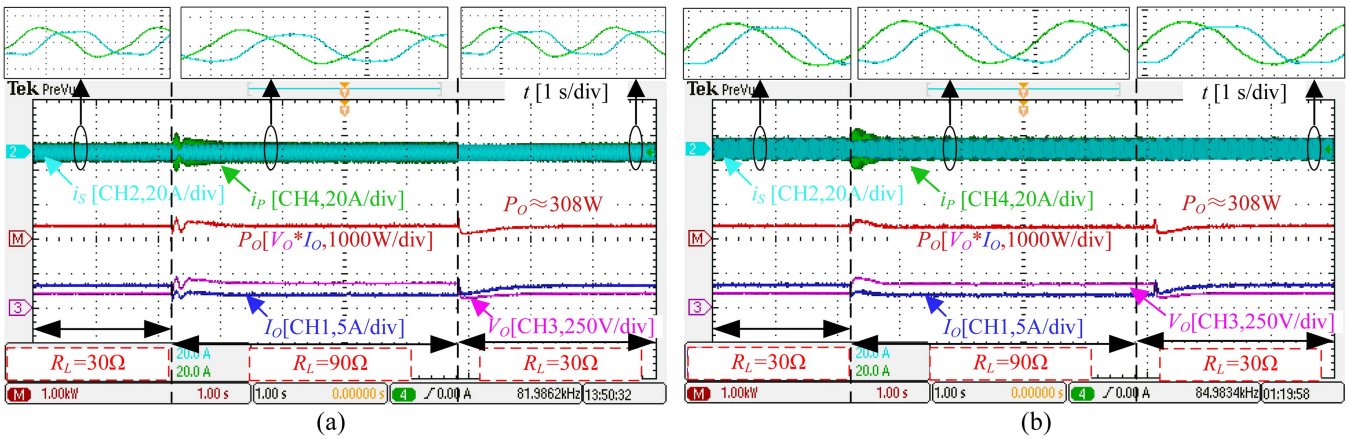

Fig. 22. Transient waveforms against step load change under different coupling coefficients. (a) $k = 0.3$. (b) $k = 0.16$.

change, and it is fixed at 0.95 via the inner loop control. The output power P_O is tightly regulated as 308 W via the outer loop control.

To verify that the proposed control strategy can maintain stability when both k and the load vary simultaneously, converter output characteristics and dc-to-dc efficiency were measured under misalignment ($k = 0.16$) and alignment conditions ($k = 0.3$), as shown in Fig. 23. The corresponding output current (dashed red curve) varies inversely with respect to the output voltage (dashed blue curve), as shown in Fig. 23(a). From Fig. 23(b), it can be observed that the output power P_O remains relatively consistent with the alignment case, approximately at a level of 308 W, even during the misalignment condition. Additionally, the converter achieves its optimal transfer efficiency, thus validating the efficacy and feasibility of the proposed wireless CP converter, even in the presence of misalignment conditions. The slight decrease in the transfer efficiency η observed in comparison to the alignment case could be primarily attributed to two factors. First, the reduction of the k during the misalignment condition leads to a decrease in efficiency. Second, a higher operating frequency is necessary to achieve the optimal equivalent ac load $R_{\mathrm{eq,opt}}$ as in the misalignment case. However, despite these factors, the dc-to-dc transfer efficiency remains at a high level of 88.7% at $k = 0.16$. This finding confirms the misalignment-tolerance range of the proposed wireless CP converter. Then, the corresponding conversion efficiency of each stage and the distribution of power loss are shown in Fig. 24. Based on the preceding analysis, the power losses incurred by the IPT can be categorized into three components: P_{FBI}, $P_{\mathrm{LCT\text{-}com}}$, and P_{SAR}. The distribution of power losses within the system can be determined by measuring four essential power parameters, namely P_{in}, P_O, $P_{O\text{-FBI}}$, and $P_{in\text{-SAR}}$. Moreover, it is noticeable that in the case of misalignment, since the operating frequency is higher than the resonant frequency point, the primary side

TABLE II
COMPARISONS WITH PREVIOUS METHODS

Reference	This work	[21]	[33]	[39]	[11]	[44]	[17]	[45]
Compensation topology	S-S	S-S	S-S	S-S	S-S	S-S	*LCC-S*	*LCC-LCC*
Single-stage	Yes	No	No	Yes	Yes	Yes	Yes	Yes
Output characteristic	Programmable CP	CV	CP	CV	CV	CP	CP	CP
Coupling range	0.16–0.30	0.12–0.25	0.09–0.15	0.21–0.38	0.26–0.28	0.23–0.26	0.26–0.30	0.16–0.32
Soft switching	Yes	No	No	No	Yes	Yes	Yes	Yes
Rating power	308 W	100 W	400 W	/	150 W	147 W	230 W	3 kW
DC–DC efficiency	88.7%–93.0%	86.4%–89.3%	82.1%–91.9%	84.8%–89.2%	85.2%–88.2%	87.4%–88.9%	88.6%–89.8%	87.5%–91.5%

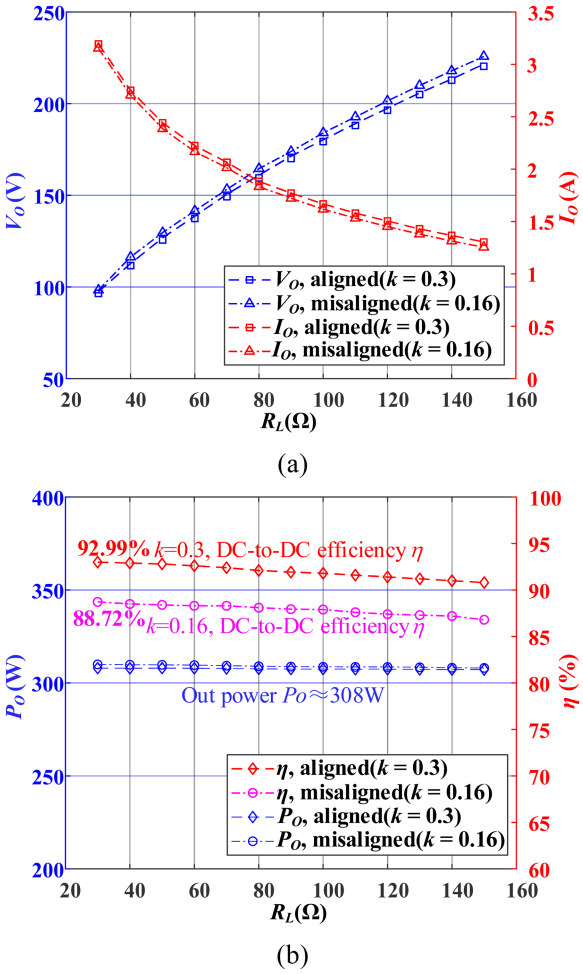

Fig. 23. Validation of the proposed method under aligned and misaligned conditions. (a) Measured output current and voltage versus R_L. (b) Measured dc-to-dc efficiency η and output power P_O versus R_L.

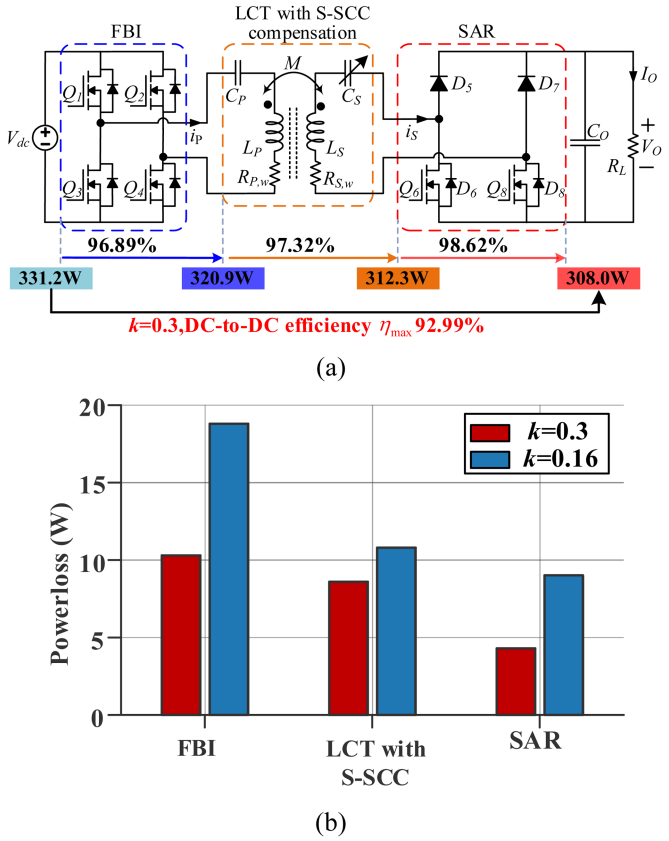

Fig. 24. Loss analysis. (a) Conversion efficiency of each stage. (b) Power loss distribution of the proposed wireless CP converter under aligned and misaligned conditions.

presents an inductive impedance, which will increase the loss of the inverter to a certain extent.

Therefore, these three sets of experiments validate the programmable CP output characteristics, optimal efficiency tracking, and CP output against variations of k and load condition.

D. Comparison With Existing Methods

To establish a more comprehensive comparison with prior studies, Table II presents various control strategies employed in the IPT system. In [33], a front-end dc–dc converter is employed to regulate the output power, resulting in the inability to achieve the optimal load-matching condition. Compared to [21] and [33], the proposed scheme in this article is a single-stage converter, which does not require an additional dc/dc converter and can reduce the cost, complexity, and power loss of the system. In

comparison to other single-stage structures such as in [11], [17], and [44], this article ensures the consistency of system output characteristics in dynamic scenarios and achieves programmable CP output. Distinct from [39] and [45], the method proposed in this article not only adjusts the output power during misalignment but also maintains impedance matching to optimize efficiency tracking as the load varies. In summary, the proposed system is based on a single-stage power-source IPT converter. The operating principle enables programmable CP output and optimal efficiency tracking against variations of coupling coefficient and load condition. Furthermore, all power switches are designed to facilitate soft-switching to reduce switching losses.

V. Conclusion

A novel control loop based on a single-stage power-source IPT converter is proposed to cope with power regulation and optimal efficiency tracking against variations of k and load condition. The operating principle is detailed and a two-loop control scheme is used to achieve a programmable CP output and track the optimal efficiency, and all power switches realize soft-switching to reduce switching losses. Furthermore, the programmable output characteristics of the IPT converter ensure that the output power capability can be maximized, rendering it suitable for applications that require battery or supercapacitor charging applications. Finally, simulation and experiment verify the correctness and feasibility of the proposed model and method. Steady-state waveforms and transient responses are experimentally measured to validate the performance. With the proposed efficiency optimization method, the IPT converter achieves an exceptionally high overall efficiency throughout the whole charging process. The peak efficiency reaches an impressive 92.99% at rated power with $k = 0.3$.

Appendix

The equivalent capacitive reactance expression for SCC can be obtained through Section II-B as

$$X_{C_{\rm SCC}} = \frac{4(\varphi-\pi)^2}{\pi^2} X_{C_S}. \tag{A1}$$

This equivalent capacitance $C_{\rm scc}$ is further obtained as

$$C_{\rm SCC} = \frac{\pi^2}{4(\varphi-\pi)^2} C_S. \tag{A2}$$

Fig. 25 shows the curve of $C_{\rm scc}$ versus the control angle φ. It can be observed that $C_{\rm scc}$ can be modulated from a nominal reactance C_s to infinity as φ is varied from 0.5π to π. Thus there exists a minimum value for $C_{\rm scc}$, i.e., $C_{\rm scc,min} = C_s$. If $C_{\rm scc}$ is guaranteed to operate properly at the minimum value C_s, then the corresponding equivalent capacitance value $C_{\rm scc}$ can be obtained by modulating the control angle φ for all other operating conditions.

The SCC needs to ensure that the secondary circuit is in resonance over the entire operating frequency range to ensure that one of the necessary conditions for optimal efficiency is satisfied. The reactance of the secondary side from the equivalent circuit model in Fig. 5 needs to satisfy $X_{S,\rm opt} = 0$, which is given by

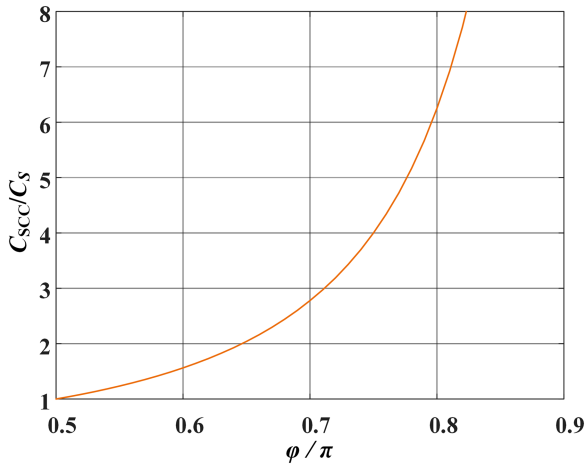

Fig. 25. Equivalent capacitance $C_{\rm scc}$ of the SCC versus control angle φ.

$$X_{S,opt} = \omega L_S - \frac{1}{\omega C_{\rm SCC}} + X_{eq} = 0. \tag{A3}$$

Therefore, the $C_{\rm scc}$ can be estimated by

$$C_{\rm SCC} = \frac{1}{\omega^2 L_S + \omega X_{\rm eq}} \left(X_{\rm eq} < 0\right). \tag{A4}$$

From (A4), a minimum $C_{\rm scc,min}$ exists when $\omega = \omega_{\max}$ and $X_{\rm eq} = 0$ (i.e., $\theta = 0°$) can be obtained

$$C_{\rm SCC} \geq \frac{1}{\omega_{\max}^2 L_S}. \tag{A5}$$

In summary, the value of C_s can be determined as (A6). It can satisfy that the secondary reactance can be resistive under the whole frequency and load range variation

$$C_S = \frac{1}{\omega_{\max}^2 L_S}. \tag{A6}$$

References

[1] G. A. Covic and J. T. Boys, "Inductive power transfer," *Proc. IEEE*, vol. 101, no. 6, pp. 1276–1289, Jun. 2013.
[2] S. Y. R. Hui, W. Zhong, and C. K. Lee, "A critical review of recent progress in mid-range wireless power transfer," *IEEE Trans. Power Electron.*, vol. 29, no. 9, pp. 4500–4511, Sep. 2014.
[3] D. Patil, M. K. McDonough, J. M. Miller, B. Fahimi, and P. T. Balsara, "Wireless power transfer for vehicular applications: Overview and challenges," *IEEE Trans. Transp. Electrific.*, vol. 4, no. 1, pp. 3–37, Mar. 2018.
[4] S. Y. Hui, "Planar wireless charging technology for portable electronic products and Qi," *Proc. IEEE*, vol. 101, no. 6, pp. 1290–1301, Jun. 2013.
[5] J. T. Boys and G. A. Covic, "The inductive power transfer story at the University of Auckland," *IEEE Circuits Syst. Mag.*, vol. 15, no. 2, pp. 6–27, Apr. 2015.
[6] C. Liu, C. Jiang, J. Song, and K. T. Chau, "An effective sandwiched wireless power transfer system for charging implantable cardiac pacemaker," *IEEE Trans. Ind. Electron.*, vol. 66, no. 5, pp. 4108–4117, May 2019.
[7] Z. Yan et al., "Frequency optimization of a loosely coupled underwater wireless power transfer system considering eddy current loss," *IEEE Trans. Ind. Electron.*, vol. 66, no. 5, pp. 3468–3476, May 2019.
[8] K. Zhang, Y. Ma, Z. Yan, Z. Di, B. Song, and A. P. Hu, "Eddy current loss and detuning effect of seawater on wireless power transfer," *IEEE J. Emerg. Sel. Topics Power Electron.*, vol. 8, no. 1, pp. 909–917, Mar. 2020.

[9] Y. Chen, Z. Kou, Y. Zhang, Z. He, R. Mai, and G. Cao, "Hybrid topology with configurable charge current and charge voltage output-based WPT charger for massive electric bicycles," *IEEE J. Emerg. Sel. Topics. Power Electron.*, vol. 6, no. 3, pp. 1581–1594, Sep. 2018.

[10] Y. Chen et al., "Variable-parameter T-circuit-based IPT system charging battery with constant current or constant voltage output," *IEEE Trans. Power Electron.*, vol. 35, no. 2, pp. 1672–1684, Feb. 2020.

[11] Z. Huang, S. C. Wong, and C. K. Tse, "An inductive-power-transfer converter with high efficiency throughout battery-charging process," *IEEE Trans. Power Electron.*, vol. 34, no. 10, pp. 10245–10255, Oct. 2019.

[12] I. W. Iam et al., "Constant-frequency and noncommunication-based inductive power transfer converter for battery charging," *IEEE J. Emerg. Sel. Topics Power Electron.*, vol. 10, no. 2, pp. 2147–2162, Apr. 2022.

[13] Y. Chen et al., "A hybrid inductive power transfer system with misalignment tolerance using quadruple-D quadrature pads," *IEEE Trans. Power Electron.*, vol. 35, no. 6, pp. 6039–6049, Jun. 2020.

[14] R. Tanikawa and H. Le, "Constant power battery charger," WO1996037941A1, Nov. 28, 1996.

[15] D. Mishra, S. De, and K. R. Chowdhury, "Charging time characterization for wireless RF energy transfer," *IEEE Trans. Circuits Syst. II, Express Briefs*, vol. 62, no. 4, pp. 362–366, Apr. 2015.

[16] Z. Huang, S. C. Wong, and C. K. Tse, "Design of a single-stage inductive power transfer converter for efficient EV battery charging," *IEEE Trans. Veh. Technol.*, vol. 66, no. 7, pp. 5808–5821, Jul. 2017.

[17] I. W. Iam, C. K. Choi, C. S. Lam, P. I. Mak, and R. P. Martins, "A constant-power and optimal-transfer-efficiency wireless inductive power transfer converter for battery charger," *IEEE Trans. Ind. Electron.*, vol. 71, no. 1, pp. 450–461, Jan. 2024.

[18] V. Z. Barsari, D. J. Thrimawithana, and G. A. Covic, "An inductive coupler array for in-motion wireless charging of electric vehicles," *IEEE Trans. Power Electron.*, vol. 36, no. 9, pp. 9854–9863, Sep. 2021.

[19] J. Tang, Y. Liu, and N. Sharma, "Modeling and experimental verification of high-frequency inductive brushless exciter for electrically excited synchronous machines," *IEEE Trans. Ind. Appl.*, vol. 55, no. 5, pp. 4613–4623, Sep./Oct. 2019.

[20] H. Kanazawa, H. Uwai, S. Kiuchi, and H. Matsumoto, "Receiver-position-based unbalanced-current control for a three-to single-phase wireless power transfer system for AGVs," *IEEE Trans. Ind. Electron.*, vol. 70, no. 4, pp. 3245–3256, Apr. 2023.

[21] Z. Huang, S. C. Wong, and C. K. Tse, "Control design for optimizing efficiency in inductive power transfer systems," *IEEE Trans. Power Electron.*, vol. 33, no. 5, pp. 4523–4534, May 2018.

[22] R. Bosshard, U. Iruretagoyena, and J. W. Kolar, "Comprehensive evaluation of rectangular and double-D coil geometry for 50 kW/85 kHz IPT system," *IEEE J. Emerg. Sel. Topics Power Electron.*, vol. 4, no. 4, pp. 1406–1415, Dec. 2016.

[23] H. Jafari, T. O. Olowu, M. Mahmoudi, and A. Sarwat, "Optimal design of IPT bipolar power pad for roadway-powered EV charging systems," *IEEE Can. J. Elect. Comput. Eng.*, vol. 44, no. 3, pp. 350–355, Jul. 2021.

[24] A. Zaheer, H. Hao, G. A. Covic, and D. Kacprzak, "Investigation of multiple decoupled coil primary pad topologies in lumped IPT systems for interoperable electric vehicle charging," *IEEE Trans. Power Electron.*, vol. 30, no. 4, pp. 1937–1955, Jun. 2015.

[25] S. Kim, G. A. Covic, and J. T. Boys, "Tripolar pad for inductive power transfer systems for EV charging," *IEEE Trans. Power Electron.*, vol. 32, no. 7, pp. 5045–5057, Sep. 2017.

[26] Z. Luo, S. Nie, M. Pathmanathan, and P. W. Lehn, "Exciter-quadrature-repeaters transmitter for wireless electric vehicle charging with high lateral misalignment tolerance and low EMF emission," *IEEE Trans. Transp. Electrific.*, vol. 7, no. 4, pp. 2156–2167, Dec. 2021.

[27] Y. Chen, S. He, B. Yang, S. Chen, Z. He, and R. Mai, "Reconfigurable rectifier-based detuned series-series compensated IPT system for anti-misalignment and efficiency improvement," *IEEE Trans. Power Electron.*, vol. 38, no. 2, pp. 2720–2729, Feb. 2023.

[28] Y. Chen et al., "A clamp circuit-based inductive power transfer system with reconfigurable rectifier tolerating extensive coupling variations," *IEEE Trans. Power Electron.*, vol. 39, no. 2, pp. 1942–1946, Feb. 2024.

[29] B. Yang et al., "A clamped IPT system with adaptive mode switching against large coupling variations," *IEEE Trans. Power Electron.*, vol. 38, no. 9, pp. 11694–11704, Sep. 2023.

[30] X. Qu, Y. Yao, D. Wang, S. C. Wong, and C. K. Tse, "A family of hybrid IPT topologies with near load-independent output and high tolerance to pad misalignment," *IEEE Trans. Power Electron.*, vol. 35, no. 7, pp. 6867–6877, Jul. 2020.

[31] G. Li, Z. Yao, S. Luo, and H. Ma, "A hybrid IPT system implementing misalignment tolerance and constant current output with primary intermediate coil," *IEEE J. Emerg. Sel. Topics Power Electron.*, vol. 10, no. 6, pp. 7797–7807, Dec. 2022.

[32] L. Zhao, D. J. Thrimawithana, U. K. Madawala, A. P. Hu, and C. C. Mi, "A misalignment-tolerant series-hybrid wireless EV charging system with integrated magnetics," *IEEE Trans. Power Electron.*, vol. 34, no. 2, pp. 1276–1285, Feb. 2019.

[33] H. Zhu, B. Zhang, and L. Wu, "Output power stabilization for wireless power transfer system employing primary-side-only control," *IEEE Access*, vol. 8, pp. 63735–63747, 2020.

[34] M. Kim, D. M. Joo, and B. K. Lee, "Design and control of inductive power transfer system for electric vehicles considering wide variation of output voltage and coupling coefficient," *IEEE Trans. Power Electron.*, vol. 34, no. 2, pp. 1197–1208, Feb. 2019.

[35] Z. Li, C. Zhu, J. Jiang, K. Song, and G. Wei, "A 3-kW wireless power transfer system for sightseeing car supercapacitor charge," *IEEE Trans. Power Electron.*, vol. 32, no. 5, pp. 3301–3316, May 2017.

[36] Y. Yang, W. Zhong, S. Kiratipongvoot, S. C. Tan, and S. Y. R. Hui, "Dynamic improvement of series–series compensated wireless power transfer systems using discrete sliding mode control," *IEEE Trans. Power Electron.*, vol. 33, no. 7, pp. 6351–6360, Jul. 2018.

[37] K. Li, S. C. Tan, and S. Y. R. Hui, "Dynamic response and stability margin improvement of wireless power receiver systems via right-half-plane zero elimination," *IEEE Trans. Power Electron.*, vol. 36, no. 10, pp. 11196–11207, Oct. 2021.

[38] T. Diekhans and R. W. De Doncker, "A dual-side controlled inductive power transfer system optimized for large coupling factor variations and partial load," *IEEE Trans. Power Electron.*, vol. 30, no. 11, pp. 6320–6328, Nov. 2015.

[39] I. Karakitsios, F. Palaiogiannis, A. Markou, and N. D. Hatziargyriou, "Optimizing the energy transfer, with a high system efficiency in dynamic inductive charging of EVs," *IEEE Trans. Veh. Technol.*, vol. 67, no. 6, pp. 4728–4742, Jun. 2018.

[40] Q. Chen, L. Jiang, J. Hou, X. Ren, and X. Ruan, "Research on bidirectional contactless resonant converter for energy charging between EVs," in *Proc. 39th Annu. Conf. IEEE Ind. Electron. Soc.*, Vienna, Austria, 2013, pp. 1236–1241.

[41] Z. Huang, D. Wang, and X. Qu, "A novel IPT converter with current-controlled semi-active rectifier for efficiency enhancement throughout supercapacitor charging process," *IEEE J. Emerg. Sel. Topics. Power Electron.*, vol. 10, no. 2, pp. 2201–2209, Apr. 2022.

[42] Y. Zhang, T. Kan, Z. Yan, and C. C. Mi, "Frequency and voltage tuning of series–series compensated wireless power transfer system to sustain rated power under various conditions," *IEEE J. Emerg. Sel. Topics Power Electron.*, vol. 7, no. 2, pp. 1311–1317, Jun. 2019.

[43] W. Liu, K. T. Chau, C. H. T. Lee, C. Jiang, W. Han, and W. H. Lam, "A wireless dimmable lighting system using variable-power variable-frequency control," *IEEE Trans. Ind. Electron.*, vol. 67, no. 10, pp. 8392–8404, Oct. 2020.

[44] Z. Huang, C. S. Lam, P. I. Mak, R. P. D. S. Martins, S. C. Wong, and C. K. Tse, "A single-stage inductive-power-transfer converter for constant-power and maximum-efficiency battery charging," *IEEE Trans. Power Electron.*, vol. 35, no. 9, pp. 8973–8984, Sep. 2020.

[45] Z. Luo, Y. Zhao, M. Xiong, X. Wei, and H. Dai, "A self-tuning LCC/LCC system based on switch-controlled capacitors for constant-power wireless electric vehicle charging," *IEEE Trans. Ind. Electron.*, vol. 70, no. 1, pp. 709–720, Jan. 2023.

[46] K. Colak, E. Asa, M. Bojarski, D. Czarkowski, and O. C. Onar, "A novel phase-shift control of semibridgeless active rectifier for wireless power transfer," *IEEE Trans. Power Electron.*, vol. 30, no. 11, pp. 6288–6297, Nov. 2015.

[47] W. Gu and K. Harada, "A new method to regulate resonant converters," *IEEE Trans. Power Electron.*, vol. 3, no. 4, pp. 430–439, Oct. 1988.

[48] Y. Yang, W. Zhong, S. Kiratipongvoot, S. C. Tan, and S. Y. R. Hui, "Dynamic improvement of series-series compensated wireless power transfer systems using discrete sliding mode control," *IEEE Trans. Power Electron.*, vol. 33, no. 7, pp. 6351–6360, Jul. 2018.

Bowei Zou (Graduate Student Member, IEEE) received the B.Eng. degree in electrical and intelligent engineering and the M.Eng. degree in electrical engineering from Xiangtan University, Xiangtan, China, in 2018 and 2021, respectively. He is currently working toward the Ph.D. degree in power electronics with the Shien-Ming Wu School of Intelligent Engineering, South China University of Technology, Guangzhou, China.

His research interests include wireless power transfer and power electronics.

Zhicong Huang (Senior Member, IEEE) received the B.Eng. degree in electrical engineering and automation and M.Eng. degree in mechanical and electronic engineering from Huazhong University of Science and Technology, Wuhan, China, in 2010 and 2013, respectively, and the Ph.D. degree in power electronics from The Hong Kong Polytechnic University, Hong Kong, in 2018.

He is currently an Associate Professor with the Shien-Ming Wu School of Intelligent Engineering, South China University of Technology, Guangzhou, China. His research interests include power electronics techniques in electric vehicles and power systems.

Dr. Huang was the recipient of the Outstanding Reviewer Award from the IEEE TRANSACTIONS ON POWER ELECTRONICS in 2021.